Dalton Transactions

PAPER

View Article Online
View Journal

Cite this: DOI: 10.1039/d5dt02366a

Structure–activity insights into benzimidazole-based Ir(III) cyclometallated complexes for cancer therapy

Eva Morales-Pioz,[a] Mónica Martínez,[b] Andrea Benedi,[a] María Tejera-Ruiz,[a] Isabel Marzo,[c] M. Concepción Gimeno,[a] Ezequiel M. Vázquez-López,[b] Soledad García-Fontán*[b] and Vanesa Fernández-Moreira*[a]

Received 3rd October 2025,
Accepted 1st December 2025

DOI: 10.1039/d5dt02366a

rsc.li/dalton

A family of cyclometallated Ir(III) complexes incorporating benzimidazole-based C^N ligands and ancillary diimines with distinct functionalities, 2-(pyridin-2-yl)-1*H*-benzo[*d*]imidazole (**L1**), 4-(1*H*-benzo[*d*]imidazol-2-yl)thiazole (**L2**), di(pyridin-2-yl)amine (**L3**), [2,2′-bipyridine]-4,4′-dicarboxylic acid (**L4**), and dibutyl [2,2′-bipyridine]-4,4′-dicarboxylate (**L5**), has been synthesised. All complexes display oxygen-sensitive emission in the 477–695 nm range; however, singlet oxygen ($^1O_2$) generation, detected by fluorescence spectroscopy, was only observed for complexes **1**, **4**, and **5**, which exhibit non-structured emission bands associated with ^{3}MLCT and ^{3}LLCT transitions. In contrast, complexes **2** and **3** show structured emission profiles consistent with predominant ^{3}LC character. The complexes exhibit distinct antitumour activity in A549 cells depending on the nature of the ancillary ligand. Complex **3**, bearing an exocyclic amine donor, displayed efficient cellular uptake and significant dark cytotoxicity. Complexes **1** and **2**, featuring endocyclic benzimidazole donors, showed lower cellular accumulation and no activity in the dark. A similar trend was observed for complex **4**, while complex **5**, its esterified analogue, showed remarkable chemotherapeutic activity and high cell uptake. The different pK_a values of **2**, **3** and **4** further correlate with their internalization capacity. Upon light irradiation, complexes **2**, **3**, and **5** exhibited enhanced antiproliferative effects and induced apoptotic cell death, probably through reactive oxygen species (ROS) generation as indicated by flow cytometry. Nevertheless, only complex **2** retained phototherapeutic potential due to its low dark toxicity. Mechanistic studies revealed that complex **2** is capable of oxidising NADH under irradiation and generating H_2O_2. Overall, these results reveal clear structure–activity relationships and highlight complex **2** as a promising candidate for photodynamic therapy (PDT), while complexes **3** and **5** act predominantly as chemotherapeutic-like agents.

Introduction

Cancer remains one of the leading causes of mortality worldwide,[1] and despite remarkable progress in early diagnosis and therapeutic interventions over the past decades, the development of safer and more effective treatments continues to be an urgent medical challenge.[2] Conventional strategies such as chemotherapy, radiotherapy, and invasive surgery still represent the clinical standard of care; however, their inherent limitations, including severe adverse effects, limited tumour selectivity, and the emergence of resistance, significantly compromise patient outcomes and quality of life.

Metal-based chemotherapeutics represent one of the most significant milestones in cancer treatment,[3] exemplified by the clinical success of cisplatin and its analogues, carboplatin and oxaliplatin. These platinum(II)-based drugs exert their activity through covalent DNA binding, ultimately triggering apoptosis.[4] Despite their efficacy, their clinical utility is limited by acquired resistance, nephrotoxicity, neurotoxicity, and, critically, poor selectivity toward malignant cells. These drawbacks underscore the need for innovative therapeutic approaches capable of combining high tumour specificity with reduced systemic toxicity.

In this context, phototherapy and in particular, photodynamic therapy (PDT) has emerged as a promising, minimally invasive therapeutic modality.[5] PDT relies on the administration of a photosensitizer (PS), which is selectively activated by light of an appropriate wavelength in the presence of mole-

---

[a] *Instituto de Síntesis Química y Catálisis Homogénea (ISQCH), CSIC-Universidad de Zaragoza, Pedro Cerbuna 12, 50009 Zaragoza, Spain. E-mail: vanesa@unizar.es*
[b] *Inorganic Chemistry Department, University of Vigo, As Lagoas, Marcosende, 36310 Vigo, Spain*
[c] *Department of Biochemistry, Molecular and Cell Biology, University of Zaragoza, 50009 Zaragoza, Spain*

cular oxygen, leading to the *in situ* generation of reactive oxygen species (ROS), primarily singlet oxygen ($^1O_2$).[6] The spatiotemporal control conferred by light irradiation provides a unique advantage in selectively targeting diseased tissues while minimizing systemic toxicity. PDT is clinically approved for the treatment of certain cancers (*e.g.*, non-small cell lung carcinoma, head and neck malignancies) as well as dermatological and ophthalmological conditions. Nevertheless, the therapeutic impact of PDT is still constrained by the limited availability of photosensitizers[7] with favourable photophysical properties, efficient tumour accumulation, and reduced dark toxicity. Thus, the design of next-generation PSs remains a central research goal.

In recent years, metal-based photosensitizers have gained increasing attention as novel PDT agents. Complexes with a d^6 electronic configuration, particularly those of Ru(II) and Ir(III), offer photophysical properties superior to those of traditional porphyrin-based PSs.[8] A notable example is TLD1433, a Ru(II) polypyridyl complex currently in phase II clinical trials for bladder cancer, which represents the first metal-based photosensitizer to enter advanced clinical evaluation.[9] This success has stimulated considerable interest in the design of other d^6 complexes, especially Ir(III) derivatives, as tunable and potent PDT candidates.[10–13]

Among the different families of coordination compounds, cyclometallated Ir(III) complexes stand out owing to their long-lived triplet excited states, high intersystem crossing efficiencies, and excellent photostability.[14,15] Their strong spin–orbit coupling facilitates efficient triplet energy transfer to molecular oxygen, enabling robust $^1O_2$ generation. Importantly, their modular architecture allows fine-tuning of their absorption/emission properties, redox behaviour, solubility, subcellular localisation, and cytotoxicity through subtle ligand modifications.[16,17]

To date, a large number of Ir(III) complexes have been investigated as photosensitizers (PSs), most of them incorporating canonical C^N ligands such as phenylpyridine or benzo[*h*]quinoline derivatives.[18–20] Among the many examples reported in the literature, Fig. 1 highlights three representative complexes: two previously developed by our group (**A** and **B**)[21,22] and one reported by He and co-workers (**C**).[23] These systems illustrate the versatility of this family of Ir(III) compounds, which have shown potential not only in photodynamic therapy (PDT) but also as chemotherapeutic agents and fluorescent probes for bioimaging. Within this context, benzimidazole-based scaffolds offer an attractive alternative due to their extended π-conjugation, electronic versatility, and ability to engage in biological interactions.[24] Their incorporation into Ir(III) architectures as C^N ligands, in combination with suitable N^N ancillary ligands, provides a powerful strategy to modulate both photophysical behaviour and biological activity. Recent studies have highlighted the therapeutic potential of benzimidazole-containing Ir(III) complexes: for example, Gandía-Herrero and co-workers reported a mitochondria-targeting Ir(III) complex with potent *in vitro* anticancer activity and low toxicity toward normal cells (complex **D**, Fig. 1)[25] while Ruiz and colleagues systematically explored how different benzimidazole substitutions influence photophysical and biological responses,[26,27] underscoring the versatility of this scaffold for therapeutic design, (complex **E**, Fig. 1).

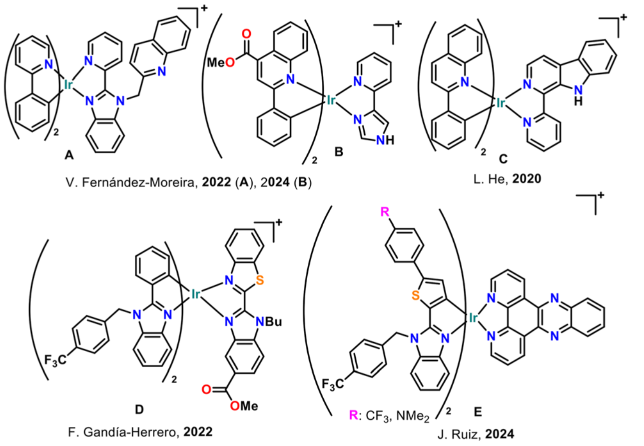

Fig. 1 Examples of biologically active cyclometallated Ir(III) complexes.[21–23,25,26]

In the present work, we investigate the impact of ancillary ligand variation on the photophysical and biological properties of a family of cyclometallated Ir(III) complexes bearing a benzimidazole-based C^N ligand. Specifically, we compare ancillary ligands featuring (a) exocyclic and (b) endocyclic amines with those containing (c) carboxylic acid groups and (d) their ester derivatives (**L1–L5**, Fig. 2).

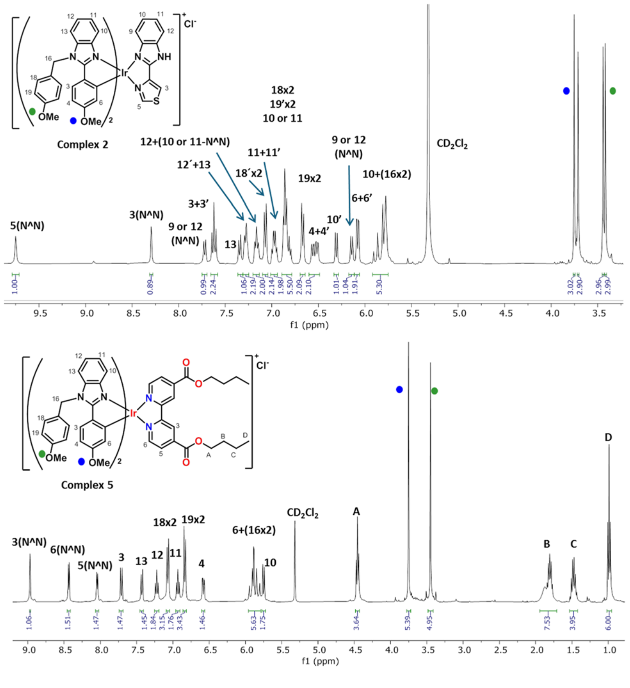

Fig. 2 ^{1}H-NMR spectra (400 MHz, CD_2Cl_2, 25 °C) of complexes **2** (top) and **5** (bottom).

Amine-based motifs, including β-carbolines and benzimidazoles, are known for their pH-dependent photophysical properties[28] and their propensity to facilitate lysosomal targeting, thereby enhancing organelle-specific accumulation.[28,29] Conversely, free carboxylates suffer from poor membrane permeability due to their negative charge at physiological pH, while esterification offers a classical strategy to improve lipophilicity and cellular uptake.[30]

By systematically evaluating these structural variations, we aim to establish clear structure–activity relationships linking ancillary ligand functionalities with cellular uptake, subcellular localization, and photodynamic efficacy. These insights will provide valuable design principles for the rational development of next-generation Ir(III)-based photosensitizers with enhanced selectivity and therapeutic performance.

Results and discussion

Design and synthesis of complexes 1–5

Given the structural versatility of benzimidazole derivatives, which offer multiple sites for derivatization that significantly influence their biological and photophysical properties,[31] the ligand 1-(4-methoxybenzyl)-2-(4-methoxyphenyl)-1*H*-benzo[*d*]imidazole was specifically selected. This choice is justified by the electron-donating character of the methoxy substituents, which modulate the excited-state energies of Ir(III) complexes by destabilising the HOMO orbitals and thereby inducing a red shift in the optical properties toward a more favourable spectral region for PDT applications.[32] Furthermore, the enhanced lipophilicity and aromaticity introduced by the methoxybenzyl groups are expected to facilitate cellular uptake and promote preferential localisation in hydrophobic subcellular compartments such as mitochondria—an attribute highly advantageous for both PDT and bioimaging.[33,34]

The target benzimidazole derivative was synthesized in good yield *via* the condensation of 4-methoxybenzaldehyde, *o*-phenylenediamine, and hexafluoroisopropyl alcohol (HFIP) (Scheme 1), following the procedure described by Chebolu *et al.*[35] Subsequently, a family of novel cyclometallated Ir(III) complexes of the general formula [Ir(C^N)$_2$(L)]Cl was prepared, where the C^N ligand corresponds to the newly obtained benzimidazole derivative, and L represents a series of diimine ancillary ligands. The selected diimines include: 2-(pyridin-2-yl)-1*H*-benzo[*d*]imidazole (**L1**), 4-(1*H*-benzo[*d*]imidazol-2-yl)thiazole (**L2**), di(pyridin-2-yl)amine (**L3**), [2,2′-bipyridine]-4,4′-dicarboxylic acid (**L4**), and dibutyl[2,2′-bipyridine]-4,4′-dicarboxylate (**L5**). This strategy afforded five novel complexes, hereafter referred to as **1–5**, Schemes 1, S1 and Fig. S1.

The synthesis was carried out using a well-established two-step protocol: (i) formation of the chloro-bridged iridium(III) dimer,[36] and (ii) cleavage of the dimer with subsequent coordination of the diimine ligand. Specifically, the chloro-bridged dimer [Ir(C^N)$_2$Cl]$_2$ was generated by refluxing $IrCl_3 \cdot nH_2O$ with 2–2.5 equivalents of the cyclometallated ligand in a 3 : 1 mixture of ethoxyethanol : water. In the second step, this intermediate was treated with two equivalents of the corresponding diimine ligand (**L1–L5**) under reflux in a CH_2Cl_2/MeOH mixture, affording the desired cationic complexes [Ir(C^N)$_2$(**L1–L5**)]Cl. The products were isolated as microcrystalline solids by precipitation with diethyl ether.

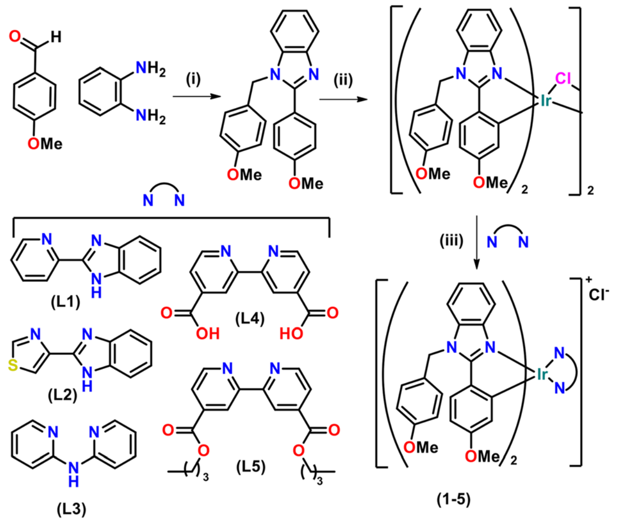

Scheme 1 Synthetic route for the preparation of **1–5**. (i) 4-Methoxybenzaldehyde, *o*-phenylenediamine, HFIP (2 : 1 : 3), r.t., 4 h. (ii) 1-(4-Methoxybenzyl)-2-(4-methoxyphenyl)-1*H*-benzo[*d*]imidazole, etoxyethanol : H_2O (8 : 1), 135 °C, 24 h; (iii) Ir-dimer, **L1–L5**, CH_2Cl_2 : MeOH (2 : 1), 60 °C, 24 h. Yields: 57% (**1**), 51% (**2**), 50.8% (**3**), 45% (**4**), 46% (**5**).

All complexes were thoroughly characterised by multinuclear NMR spectroscopy (^{1}H, ^{13}C{^{1}H}), supported by 2D techniques (COSY, HSQC, and HMBC) to facilitate unambiguous resonance assignment (Fig. S2–S26). Complexes **1** and **2**, bearing the non-symmetrical diimine ligands **L1** and **L2**, exhibited significantly more complex ^{1}H and ^{13}C NMR spectra compared to **3–5**, see Fig. 2. The asymmetry of **L1** and **L2** led to distinct resonances for each proton and carbon of both C^N ligands, complicating spectral assignment of complexes **1** and **2**. For all complexes (**1–5**), characteristic downfield and shielding effects consistent with coordination were observed. For instance, the proton at C(6) of the C^N ligand exhibited substantial shielding upon metalation, resonating between 6.30 and 5.75 ppm.

Additionally, the CH(10) protons of C^N ligands, spatially oriented toward the π-system of the aromatic diimine ligands (**L1–L5**), consistently appeared around 6.5 ppm, indicative of intramolecular C–H/π interactions and confirming the coordination environment. In the specific case of **1** and **2**, CH(10) of each C^N ligand exhibited a more pronounced splitting (CH(10)-A and CH(10)-B), again reflecting the reduced symmetry imparted by **L1** and **L2** in comparison with **L3–L5**. The ^{13}C NMR spectra followed analogous trends, with clear perturbations in the resonances of both the cyclometallated and ancillary ligand carbons.

Further confirmation of the molecular formulations was obtained by high-resolution electrospray ionization mass spectrometry (HRMS-ESI), which displayed the expected $[M - Cl]^+$ molecular ion peaks, while the analytical purity of all complexes was verified by elemental analysis, with values in good agreement with the calculated compositions (see Experimental section in SI and Fig. S27–S31).

Single crystals of complex **1** suitable for X-ray diffraction analysis were obtained by slow vapor diffusion of pentane solution into a dichloromethane solution of the complex. Crystallographic data and refinement parameters are summarized in Table S1. Complex **1** crystallizes in the monoclinic crystal system with space group *C*2/*c*, and the asymmetric unit contains one $[Ir(C\text{^}N)_2(\mathbf{L1})]Cl$ molecule accompanied by a co-crystallized dichloromethane solvent molecule. The unit cell comprises eight formula units of complex **1**, arranged as a racemic mixture of both Λ and Δ enantiomers. The molecular structure of **1** confirms the expected octahedral coordination geometry typical of cyclometallated Ir(III) complexes, Fig. 3. Two 1-(4-methoxybenzyl)-2-(4-methoxyphenyl)-1*H*-benzo[*d*]imidazolyl ligands act in a C^N bidentate fashion, binding through the benzimidazolyl nitrogen atoms (N11 and N21), which are disposed in mutually *trans* positions. Accordingly, the two cyclometallated 4-methoxyphenyl carbons occupy sites *trans* to the chelating diimine ligand, in this case 2-(pyridin-2-yl)-1*H*-benzo[*d*]imidazole (**L1**), thereby completing the distorted octahedral geometry around Ir(III). Bond metric analysis highlights the strong *trans* influence exerted by the cyclometallated aryl donors. This is reflected in longer Ir–N distances for the pyridyl–benzimidazole ligand (Ir1–N31: 2.142(8) Å; Ir1–N32: 2.192(9) Å), compared to the Ir–N bond lengths for the C^N ligands (Ir1–N11: 2.061(8) Å; Ir1–N21: 2.037(8) Å). The constrained bite angle of the pyridyl–benzimidazole (N31–Ir–N32: 76.2(3)°) further enforces a distortion from the ideal octahedral disposition (90°), Fig. 3 and Tables S2, S3. The chloride anion is associated with the complex cation through a hydrogen interaction involving the N32–H group of the imidazole of L1 (N(32)–H(3N)···Cl(1) = 0.88, 2.24, 3.035(9) Å and 150.0°). Other weak interactions involving aromatic C–H groups as hydrogen donors and O atoms of ether groups as acceptors, probably contribute to crystal packing, Table S4.

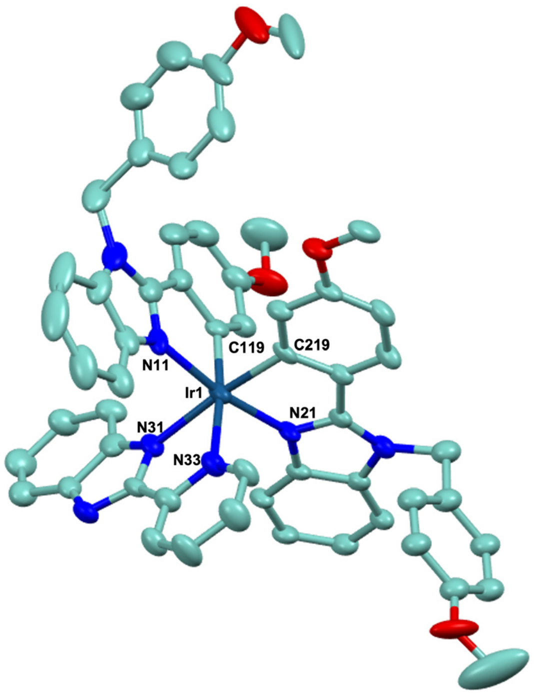

Fig. 3 Molecular structure of complex **1** showing ellipsoids at the 30% probability level. Hydrogen atoms and counter ion are omitted for clarity. Most relevant bond distances (Å) and angles (°): Ir1–C119: 1.994(10), Ir1–C219: 2.009(9), Ir1–N11: 2.061(8), Ir1–N21: 2.037(8), Ir1–N31: 2.142(8), Ir1–N33: 2.192(9); N11–Ir1–N21: 170.5(3), N33–Ir1–N31: 76.2(3).

Photophysical study

The optical properties of complexes **1–5** were investigated in DMSO solution at room temperature, and the relevant data are summarised in Table 1. The absorption spectra show intense bands around 305 nm ($\varepsilon \approx 4.5 \times 10^4\ M^{-1}\ cm^{-1}$), which are assigned to ligand-centred (LC) π–π* transitions within the C^N and N^N ligands.

Lower-energy shoulders of moderate intensity appear between 342 and 368 nm. In addition, broad absorptions between 390 and 510 nm are observed, characteristic of metal-to-ligand (MLCT) and ligand-to-ligand (LLCT) charge-transfer transitions, involving both singlet and triplet origin (^{1}MLCT/^{3}MLCT; dπ → π*(N^N) and ^{1}LLCT/^{3}LLCT; π(C^N) → π*(N^N)). Notably, complexes **4** and **5** display additional absorption bands beyond 500 nm with long tails, reflecting stabilization of the accepting frontier orbitals, typically localized on the diimine ligands.[31] This is consistent with the stronger acceptor character of **L4** and **L5** in **4** and **5** compared to those in **1–3**. The stability of **1–5** in DMSO solution was confirmed by monitoring their UV–Vis absorption spectra over 48 h, which showed no significant changes (Fig. S32–S34).

All complexes are emissive in aerated DMSO solution at 298 K, with maxima covering the orange-to-deep red region, Fig. 4 and S35–S37. Complex **1** exhibits a broad emission centred at 545 nm, while **2** and **3** display structured bands between 477–551 nm, with evident vibronic progression indicative of a larger ligand-centred (LC) contribution[37] to their emissive triplet states and following the trend of similar complexes described by Espino and coworkers.[38] Complex **4** emits at 569 nm, whereas **5** shows a strongly red-shifted maximum ($\lambda_{em} \approx 695$ nm), consistent with its lowest-energy absorption and suggesting an emissive state of predominant ^{3}MLCT/^{3}LLCT character stabilized by the acceptor character of **L5**. Time-resolved measurements confirm a triplet origin for the visible emissions, with lifetimes in the 70–400 ns range under air at room temperature. The photoluminescence quantum yields (Φ_{em}) in aerated DMSO vary widely, from very low for **5** ($\Phi \approx 0.3\%$) to moderate for **4** ($\Phi \approx 20\%$). Upon deoxygenation, Φ_{em} increases dramatically for all complexes (**1:** 0.9% → 55.9%; **2:** 4.5% → 74.5%; **3:** 4.8% → 73.6%; **4:** 20.0% → 60.4%; **5:** 0.3% → 2.6%), confirming efficient dynamic quenching of the triplet states by dissolved oxygen. Rate con-

Table 1 Photophysical data of **1–5** measured in DMSO and/or CH_3CN solution at 298 K

	λ_{abs}/nm (10^4 ε/dm^3 mol^{-1} cm^{-1})^a	λ_{em}/nm (λ_{exc}/nm)^a	τ^a/ns	τ^b/ns	Φ_{em} ^{a} (%)	Φ_{em} ^{c} (%)	κ_r ^{a} ($\times 10^5$, s^{-1})	κ_{nr} ^{a} ($\times 10^5$, s^{-1})	λ_{em} ($^1O_2$) (1270 nm)
1	315 (4.62), 342 (3.14), 367 (2.47), 412 (0.66)	545 (425)	304	76	0.9	55.9	0.2	32.5	Yes
2	313 (4.87), 368 (1.37), 410 (0.51)	481, 510, 551 (375)	244	40	4.5	74.5	1.8	39.1	No
3	310 (4.63), 365 (1.62), 395 (0.87)	477, 510, 550, (400)	293	21	4.8	73.6	1.6	32.5	No
4	309 (4.52), 364 (1.82), 389 (1.21), 478 (0.10), 505 (0.07)	569 (450)	394	171^d	20.0	60.4	5.1	20.3	Yes
5	308 (4.52), 361 (2.06), 390 (1.19), 450 (0.18), 529 (0.12)	695 (475)	70	75	0.3	2.6	0.4	142.4	Yes

Absorption (λ_{abs}), emission (λ_{em}), lifetimes of excited state (τ), emission quantum yields (Φ) and $^1O_2$ generation quantum yield ($^1O_2$, Φ) of compounds **1–5** in 2×10^{-5} M in DMSO or CH_3CN solutions at 298 K. ^{a} Aerated DMSO solution. ^{b} Aerated CH_3CN solution. ^{c} N_2 saturated DMSO solution. ($K_r = -K_{nr} + 1/\zeta$ and $K_{nr} = (1 - \Phi)/\zeta$).[41] ^{d} Reported lifetime value correspond to the average lifetime obtained from a biexponential fit: τ_1 = 225 ns (A_1 = 3.20 and I^1 = 144 kCnts per Chnl); τ_2 = 116 ns, (A_2 = 6.02 and I_2 = 141 kCnts per Chnl).

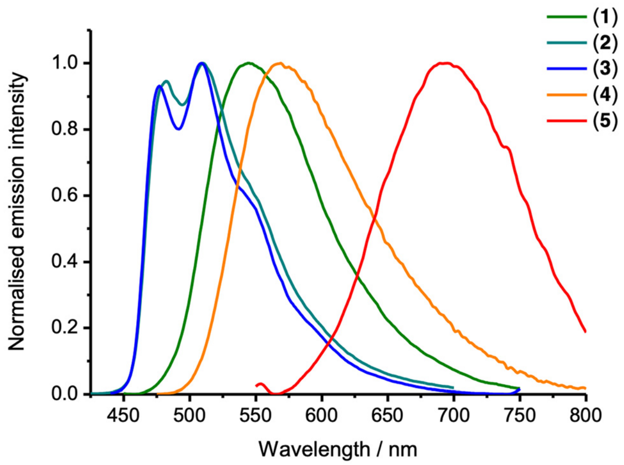

Fig. 4 Emission spectra of **1–5** in DMSO (2×10^{-5} M) at 298 K.

stant analysis shows that nonradiative decay dominates for **1–3**, and particularly for **5**, whereas **4** achieves the most favourable balance between radiative and nonradiative processes, accounting for its comparatively higher efficiency under air.

Given the strong influence of molecular oxygen on the emissive properties, the ability of complexes **1–5** to generate singlet oxygen ($^1O_2$) was investigated by time-resolved emission spectroscopy. The phosphorescence emission of $^1O_2$ is expected near 1270 nm.[39] Upon irradiation with a picosecond pulsed diode laser at 450 nm, clear emission centred at 1272 nm was observed for complexes **1**, **4**, and **5**, confirming their ability to generate $^1O_2$ (Fig. S38).

Control experiments with neat acetonitrile ruled out instrumental artefacts. In contrast, barely $^1O_2$ emission was detected for **2** and **3**. The low $^1O_2$ sensitization in complexes **2** and **3** can be attributed to the predominant LC character of their triplet excited states, which results in weaker spin–orbit coupling and significantly shorter excited-state lifetimes compared to complexes **1**, **4**, and **5**, thereby reducing the probability of efficient energy transfer to O_2.[40] As a result, even though **2** and **3** display enhanced luminescence in deoxygenated solution, they remain low effective $^1O_2$ photosensitizers in those conditions.

Antiproliferative potential and cytotoxicity

The antiproliferative activity of complexes **1–5** was assessed using MTT-reduction assay in human lung carcinoma A549 cells under both dark and photoirradiation conditions (λ = 405 nm) to evaluate their potential as chemotherapeutic and/or photodynamic agents (Table 2). Complexes **1** and **4** exhibited IC_{50} values above 50 μM and 100 μM, respectively, under both experimental conditions, indicating that these species have no antitumour activity and suggesting that they are unsuitable for therapeutic applications in either chemotherapy or PDT. In contrast, complexes **3** and **5** significantly reduce cell proliferation even in the absence of light, with IC_{50} values of 0.35 ± 0.01 μM and 2.69 ± 0.43 μM, respectively. Irradiation only slightly enhanced their antiproliferative activity, pointing to a mechanism of action more consistent with a conventional chemotherapeutic profile rather than a light-activated PDT agent. Conversely, complex **2** was essentially inactive in the dark (IC_{50} > 50 μM), but irradiation substantially improved its cell growth-inhibitory potential, reaching an IC_{50} of 1.62 ± 0.38 μM. This pronounced light-dependent activity highlights complex **2** as a promising candidate photosensitiser for PDT applications, see Table 2. To rationalise these trends, the octanol/water partition coefficients ($\log P$)[42] and cellular uptake, quantified by ICP-MS, were analysed. Even though experimental $\log P$ did not showed any trend that can be associated with the activity displayed by the complexes, the

Table 2 IC_{50} values (μM) of complexes **1–5** incubated with A549 cells. $\log P$ values of complexes **1–5**

	IC_{50}(dark)	IC_{50}(irrad.)	PI	log $_{(oct/water)}$
1	>50	>50	—	1.6
2	>50	1.62 ± 0.38	≥30	3.1
3	0.35 ± 0.01	0.025 ± 0.009	14	2.3
4	>100	>100	—	0.4
5	2.69 ± 0.43	1.38 ± 0.50	2	1.8
CisPt	9.39 ± 0.08	n.d.	—	—

Conditions: incubation for 48 h in the dark and under irradiation (405 nm, 10 min, 0.65 J cm^{-2}). PI: photocytotoxic index = IC_{50}(dark)/IC_{50}(irrad.). $\log P$ values calculated by the shake method.[42] n.d.: not determined. A549 cells from ATCC, Manassas, VA, USA.

ICP-MS assays revealed a marked correlation between internalisation and dark bioactivity, Fig. 5A.

Complexes **3** containing **L3** (di(pyridin-2-yl)amine) and **5** containing **L5** (dibutyl[2,2′-bipyridine]-4,4′-dicarboxylate) showed the highest uptake levels, correlating directly with their high dark antiproliferative activity, see Table 2 and Fig. 5A. This suggests that high cellular accumulation facilitates interactions with intracellular targets, leading to efficient cell-growth inhibition even in the absence of light. In contrast, complex **2** (**L2**, benzimidazolyl–thiazole) shows only moderate cellular uptake; however, once inside the cell and upon light irradiation, its antitumour activity increases, likely due to the generation of reactive oxygen species (ROS). Complex **1** exhibits the lowest uptake of the series. Overall, the differences in antiproliferative activity among complexes **1**, **2**, and **3** can be rationalised by the nature and acidity of their amine donors. In complex **3**, the exocyclic –NH– group of di(2-pyridyl)amine is only minimally perturbed upon metal coordination. By contrast, in complexes **1** and **2**, the endocyclic –NH– group of the benzimidazole fragment experiences a stronger electronic influence from the metal centre, which increases its acidity and favours deprotonation at physiological pH. As a result, a larger fraction of complexes **1** and **2** exists in the neutral form, which typically displays poorer cellular internalisation than the more protonated species predominant in complex **3**. This interpretation is supported by the calculated pK_a values. Complex **2**, used as a model for an endocyclic –NH– donor, exhibits a pK_a of 7.95 ± 0.08, whereas complex **3** presents a significantly higher pK_a of 10.56 ± 0.16 (Fig. S43). Accordingly, at physiological pH, a greater proportion of complex **2** is expected to be deprotonated, generating neutral species with reduced membrane permeability, consistent with previously reported Ir(III) complexes containing endocyclic –NH– donors.[43] Moreover, this trend correlates with the lower intracellular Ir levels quantified by ICP-MS for complex **2** compared with complex **3** (Fig. 5A). Many examples have been reported showing that cationic metal complexes exhibit higher cellular uptake than their neutral or anionic analogues.[44–46] Therefore, the structural features of the ancillary ligands appear decisive in governing both uptake and antitumour activity. In the case of complexes **4** and **5**, esterification of the dicarboxylate ligand **L4** into its lipophilic ester **L5** significantly enhanced cellular uptake of the complex, consistent with the increased compatibility of ester groups with the lipidic nature of cellular membranes,[30] as indicated by the greater antiproliferative character (IC_{50}(**4**) > 100 μM *vs.* IC_{50}(**5**) = 2.69 ± 0.43).

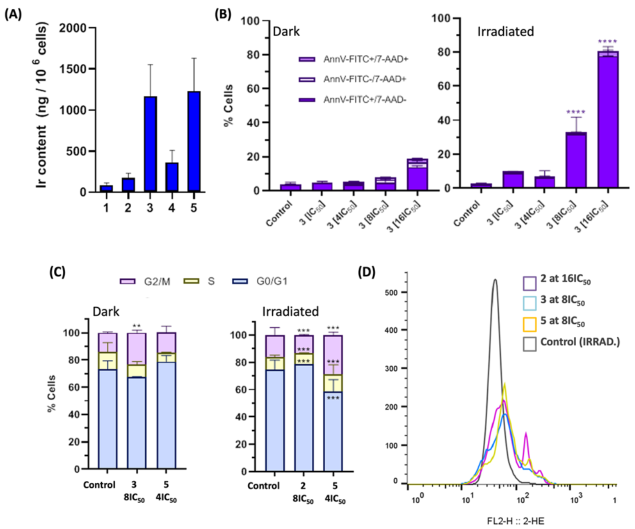

Fig. 5 (A) ICP-MS quantification of the iridium content in whole cells. Cellular uptake of complexes **1–5** incubated at 50 μM in A549 cells after 4 h incubation in the dark. (B) Flow cytometry graph of cellular death mechanism for **3** incubated with A549 for 24 h and irradiation at 405 nm for 10 min (0.65 J cm^{-2}) using Annexin V-FITC and 7-AAD as markers. (C) Distribution of cell populations in the different phases of the cell cycle after exposure to complex **2** after irradiation, complex **3** in darkness, and complex **5** under dark and irradiation conditions (10 min, 405 nm, 0.65 J cm^{-2}) at the indicated concentrations. (D) Intracellular ROS production of complexes **2**, **3** and **5** in A549 cells under irradiation at the indicated concentrations (10 min, 405 nm, 0.65 J cm^{-2}) using the DHE probe as a marker.

The mechanism of cell death was investigated for those complexes exhibiting significant reduction in cell viability by flow cytometry. Complexes **3** and **5** were analysed under dark and irradiated conditions, while complex **2** was examined only upon irradiation, Fig. 5B and S42. Annexin V-FITC and 7-AAD were used as apoptotic and necrotic markers for complexes **2** and **3**, whereas only Annexin V-FITC was used for complex **5** due to overlap of its emission profile with that of 7-AAD. Overall, these results reveal a dose-dependent cytotoxic effect for all species, which is especially evident after irradiation. Complex **3** showed as the greatest cytotoxic activity upon irradiation, with ~80% apoptosis at 16 × IC_{50}, Fig. 5B-right. However, it only induced ~20% cell death in darkness, Fig. 5B-left. A similar pattern was observed with complex **5**, as toxicity was ~20% in the dark, but increased to ~40% after irradiation at the highest concentration (Fig. S42). These responses suggest that complexes **3** and **5** display a cytostatic effect under dark conditions, while upon irradiation, the cytotoxic effect is enhanced. Finally, only the cytotoxic potential of complex **2** was assessed after irradiation, since this complex is inactive in the dark. The results indicate that it triggers apoptosis at 16 × IC_{50}, albeit less efficiently than complex **3** (~50%), Fig. 5B and S42.

To further explore the mechanism of action of the compounds, the cell cycle was analysed in those cases where an acceptable IC_{50} value was obtained, but the level of cell death detected was minimal at relatively high concentrations. Specifically, we evaluated complex **3** in darkness (8 × IC_{50}), complex **2** after irradiation (8 × IC_{50}) and complex **5** in both conditions (4 × IC_{50}).

In dark conditions, only slight changes are observed in the distribution of cell populations between the treatments and the control. An increase in the G2/M phase is registered with complex **3** compared to untreated cells, which may indicate a subtle arrest in G2/M. In contrast, complex **5** led to a small accumulation of cells in the G0/G1 phase, suggesting a slowdown in cell growth in this case, Fig. 5C-left. Interestingly, complex **5** caused an increase in the G2/M cell population after irradiation at the expense of the G0/G1 population, consistent with a modest arrest in the G2/M phase, Fig. 5C-right. Conversely, complex **2** did not alter the cell cycle profile upon light activation. The G2/M arrest identified with complexes **3** in the dark and **5** upon irradiation may partly explain the cytostatic potential of the compounds at the indicated concentrations.

Furthermore, the complexes could slow progression through all phases of the cell cycle without increasing the cell population at any single phase. This would imply a decrease in cell proliferative capacity and is aligned with our observation of increased cell size after treatments (data not shown) and subtle changes in the cell cycle profile. Since complexes **2**, **3**, and, to a lesser extent, complex **5** displayed enhanced antiproliferative activity upon irradiation, ROS generation under these conditions was evaluated by flow cytometry using dihydroethidium (DHE), which primarily detects superoxide anion ($O_2^{\bullet -}$), although it can also be oxidized by other reactive oxygen species. All three complexes promoted significant ROS production, as evidenced by a rightward shift and broadening of the fluorescence signals relative to the control experiment, Fig. 5D. Moreover, the emergence of distinct peaks at higher fluorescence intensities indicated the presence of subpopulations of cells with markedly elevated ROS levels, a phenomenon particularly pronounced for complex **3**.

Photocatalytic oxidation of NADH

The ability of complex **2** to generate reactive oxygen species under irradiation was examined by evaluating its photooxidation activity toward several biologically relevant metabolites, including NADH, glutathione (GSH), and ascorbic acid (AscH). Hydrogen peroxide test strips were used as indicators. Solutions of each molecule in phosphate-buffered saline/dimethylformamide were incubated with complex **2** and irradiated with blue light (λ = 405 nm, 0.65 J cm^{-2}) for 10 min and subsequently for 1 h. After 10 minutes of irradiation, only the NADH-containing sample yielded a detectable peroxide signal, which intensified markedly after 1 h, Fig. 6A and S44A. This selective response indicates that complex **2** efficiently and specifically photooxidizes NADH in agreement with analogous Ir(III) complexes.[47] NADH plays a central role in mitochondrial metabolism, and alterations in the NADH/NAD$^+$ ratio disrupt electron transport and ATP production and disrupt the hypoxic homeostasis of cancer cells.[48] To monitor the efficiency of NADH oxidation reaction, its UV–vis absorption spectrum was recorded in presence of complex **2**. No spectral changes occurred in the dark (Fig. S44).

Under irradiation, however, the characteristic 339 nm band progressively decreased over 1 h (Fig. 6B), consistent with the light-driven oxidation of NADH to NAD$^+$, in line with previous reports.[47,49] The photocatalytic efficiency was then quantified and complex **2** displayed a turnover frequency (TOF) of 80.8 h^{-1} after 2 minutes irradiation, see Fig. S45.

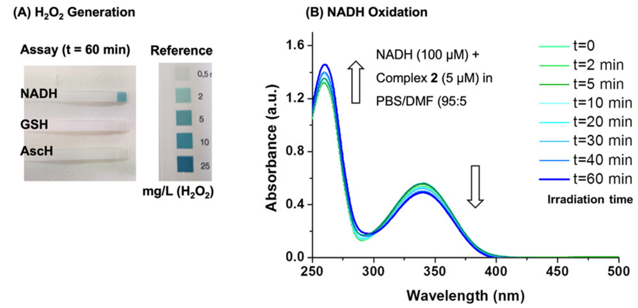

Fig. 6 (A) Detection of H_2O_2 generation after 60 min irradiation for the reaction of complex **2** (10 μM) with either NADH, GSH and AscH (1 mM). (B) Blue light-induced NADH (100 μM) oxidation by complex **2** (5 μM), monitored by UV-Vis at different time intervals in PBS/DMF (95 : 5) (v/v) mixture (light source for both experiments: 405 nm, 0.65 J cm^{-2}).

Intracellular organelle distribution

The subcellular distribution of the complexes is a key parameter in the design of metallodrugs, as it governs their mechanism of action, therapeutic efficacy, and potential side effects.[50] To gain insight into this aspect, the organelle biodistribution of complexes **1–5** was examined by fluorescence confocal microscopy.

For complexes **1** and **2**, no reliable images could be obtained, most likely due to their very low luminescence quantum yields under aerated conditions. On the contrary, complex **3** displayed clear intracellular uptake, with fluorescence distributed throughout the cytoplasm but excluded from the nucleus, Fig. 7. Upon light irradiation, the formation of intracellular bubbles was observed, consistent with optical changes detected during antiproliferative assays and indicative

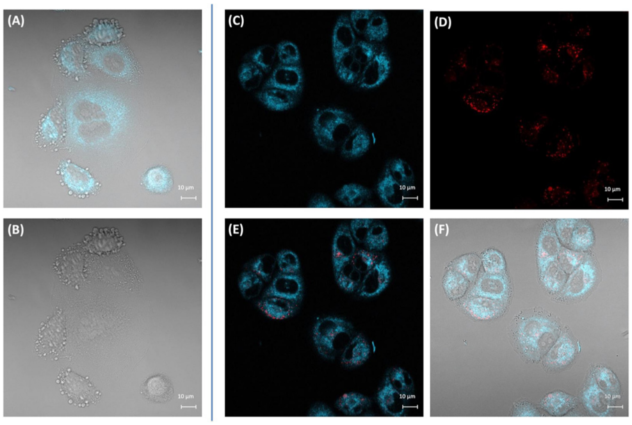

Fig. 7 (A) Confocal microscopy image of A549 incubated with **3** (6 μM) for 2 hours (laser at 405 nm, emission window (EW) was from 451 to 599 nm). (B) Phase contrast image. Confocal microscopy images of A549 incubated with **3** (6 μM) for 2 hours, followed by the addition of LysoTracker deep red (LTDR, 45 min incubation, 55 nM). (Laser at 405 nm for activating **3** and at 633 nm for LTDR, EW(**3**) = 451–599 nm and EW(LTDR) = 635–758 nm). (C) Image taken upon photoactivating complex **3**. (D) Upon photoactivating LTDR. (E) Superimposition of images C and D. (F) Superimposition of images C, D and phase contrast.

of a photocytotoxic response, see Fig. 7A, B and S46. Co-incubation with LysoTracker Deep Red (LTDR) demonstrated a lack of lysosomal accumulation, Fig. 7C–F.

Complex **4** also penetrated the cytoplasm without nuclear localization. However, partial precipitation was evident, and the weak emission signal precluded reliable determination of its organelle-specific distribution, Fig. S47. A similar behavior was observed for complex **5**, which internalized into the cytoplasm but not the nucleus, accompanied by substantial extracellular precipitation. Co-localization assays with MitoTracker green failed to provide unambiguous assignment of its subcellular target.

Conclusions

In this work, we reported the design, synthesis, and systematic evaluation of a new family of cyclometallated Ir(III) complexes featuring a benzimidazole-based C^N ligand combined with ancillary diimines of distinct functionalities; 2-(pyridin-2-yl)-1*H*-benzo[*d*]imidazole (**L1**), 4-(1*H*-benzo[*d*]imidazol-2-yl)thiazole (**L2**), di(pyridin-2-yl)amine (**L3**), [2,2′-bipyridine]-4,4′-dicarboxylic acid (**L4**), and dibutyl[2,2′-bipyridine]-4,4′-dicarboxylate (**L5**). The results underscore the critical influence of ancillary ligands in modulating photophysical properties, cellular uptake, and bioactivity. Complexes **1** and **4** were biologically inactive under both dark and irradiated conditions, whereas complexes **3** and **5** showed strong dark antitumour activity consistent with their high cellular internalization and with their overall pK_a values, identifying them as chemotherapeutic-like agents. In contrast, complex **2** stood out as the most promising PDT candidate, remaining inactive in the dark but displaying potent growth inhibition upon light exposure (IC_{50} = 1.62 ± 0.38 μM), pointing towards the importance of controlling the permeability of cyclometallated complexes when it comes to design PDT agents. Photophysical studies revealed that only complexes **1**, **4**, and **5** were efficient $^1O_2$ sensitizers, correlating with ^{3}MLCT/^{3}LLCT triplet states character. Complexes **2** and **3**, whose excited states are dominated by ^{3}LC triplet character, did not produce detectable $^1O_2$ by fluorescence spectroscopy. Nevertheless, complex **2** exhibited pronounced photoactivity, indicating that other ROS pathways or direct photodamage may contribute to its mechanism of action. In fact, H_2O_2 formation was observed upon selective photo-oxidation of NADH by complex **2**. Cell death and cell cycle analyses showed that complexes **3** and **5** exhibit cytostatic activity in the dark, while irradiation enhances the induction of apoptotic cell death, with complex **3** being the most cytotoxic (>80% of apoptosis a 16 × IC_{50}). By contrast, complex **2** is inactive in darkness but becomes moderately cytotoxic after irradiation at high concentrations. However, at low concentrations it is non-toxic and does not modify the cell cycle profile. This may be consistent with a decrease in cell growth due to a reduced progression rate through all phases of the cell cycle, without altering the distribution of cell populations across the phases. Biodistribution assay by fluorescence microscopy only allowed to distinguish internalization of **3–5** in the cytoplasm but excluded from the nucleus.

These findings assist to establish structure–activity relationships in benzimidazole-containing Ir(III) complexes, revealing how ancillary ligand design can dictate both photophysical properties and biological outcomes.

Author contributions

Conceptualization, V. F.-M.; synthesis of the ligands, E. M. P., M. M., S. G.-F., E. M. V.-L.; synthesis of the complexes, E. M. P; evaluation of the absorption, emission, stability properties, E. M. P; evaluation of excited state lifetimes, V. F.-M.; evaluation of antiproliferative activity properties, log *P*, E. M. P.; evaluation of ROS and cell death mechanism, E. M. P., A. B., I. M.; pK_a calculation and photocatalytic activity in NADH, SGH and AscH, M. T.-R.; measurement and analysis of X-Ray, M. C. G. and E. M. V.-L. Data curation, V. F.-M., E. M. P., M. C. G. and E. M. V.-L.; writing—original draft preparation, V. F.-M. and E. M. P.; writing—review and editing, all authors; supervision, V. F.-M., E. M. V.-L. and S. G.-F.; project administration, V. F.-M. Funding acquisition, V. F.-M., M. C. G., E. M. V.-L. All authors have read and agreed to the published version of the manuscript.

Conflicts of interest

There are no conflicts to declare.

Data availability

The data that support the findings of this study are available in the supplementary information (SI). Supplementary information: general measurement conditions, analysis instrumentation, experimental procedures and characterisation, photophysical studies and *in vitro* assays. See DOI: https://doi.org/10.1039/d5dt02366a.

CCDC 2492431 contains the supplementary crystallographic data for this paper.[51]

Acknowledgements

Authors thank grant PID2022-137862NB-I00 and PID2022-136861NB-I00 funded by MICIU/AEI/10.13039/501100011033 and by the European Union; grant CNS2023-143600 funded by MCINU/AEI/10.13039/501100011033 and by the European Union NextGenerationEU/PRTR. Authors also thank the Gobierno de Aragón-Fondo Social Europeo (E07_23R) and Xunta de Galicia (GRC-ED431C 2024/28) for financial support and the Spanish network OASIS (RED2022-134074-T) is also acknowledged.

References

1 F. Bray, M. Laversanne, H. Sung, J. Ferlay, R. L. Siegel, I. Soerjomataram and A. Jemal, *Ca-Cancer J. Clin.*, 2024, **74**, 229–263.

2 B. Liu, H. Zhou, L. Tan, K. T. H. Siu and X.-Y. Guan, *Signal Transduction Targeted Ther.*, 2024, **9**, 175.

3 S. Abdolmaleki, A. Aliabadi and S. Khaksar, *Coord. Chem. Rev.*, 2024, **501**, 215579.

4 D. Gibson, *Dalton Trans.*, 2009, 10681.

5 Y. Cai, T. Chai, W. Nguyen, J. Liu, E. Xiao, X. Ran, Y. Ran, D. Du, W. Chen and X. Chen, *Signal Transduction Targeted Ther.*, 2025, **10**, 115.

6 J. M. Dąbrowski, in *Advances in Inorganic Chemistry*, Elsevier, 2017, vol. 70, pp. 343–394.

7 A. M. Oluwajembola, W. D. Cleanclay, A. F. Onyia, B. N. Chikere, S. Zakari, E. Ndifreke and O. C. De Campos, *Results Chem.*, 2024, **10**, 101715.

8 B. Kar, U. Das, N. Roy and P. Paira, *Coord. Chem. Rev.*, 2023, **474**, 214860.

9 S. Monro, K. L. Colón, H. Yin, J. Roque, P. Konda, S. Gujar, R. P. Thummel, L. Lilge, C. G. Cameron and S. A. McFarland, *Chem. Rev.*, 2019, **119**, 797–828.

10 M. Redrado, A. Benedi, I. Marzo, M. C. Gimeno and V. Fernández-Moreira, *Pharmaceutics*, 2021, **13**, 1382.

11 B. Joshi and M. Shivashankar, *ACS Omega*, 2023, **8**, 43408–43432.

12 C. Jones, M. Martinez-Alonso, H. Gagg, L. Kirby, J. A. Weinstein and H. E. Bryant, *J. Med. Chem.*, 2024, **67**, 16157–16164.

13 K. Laws, A. Eskandari, C. Lu and K. Suntharalingam, *Chem. – Eur. J.*, 2018, **24**, 15205–15210.

14 F. Monti, A. Baschieri, L. Sambri and N. Armaroli, *Acc. Chem. Res.*, 2021, **54**, 1492–1505.

15 L. K. McKenzie, H. E. Bryant and J. A. Weinstein, *Coord. Chem. Rev.*, 2019, **379**, 2–29.

16 J. Sanz-Villafruela, A. Carbayo, M. Martínez-Alonso and G. Espino, *Coord. Chem. Rev.*, 2025, **534**, 216572.

17 P. Szymaszek, M. Tyszka-Czochara and J. Ortyl, *Eur. J. Med. Chem.*, 2024, **276**, 116648.

18 M.-M. Wang, X.-L. Xue, X.-X. Sheng, Y. Su, Y.-Q. Kong, Y. Qian, J.-C. Bao, Z. Su and H.-K. Liu, *RSC Adv.*, 2020, **10**, 5392–5398.

19 S. A. Sharma, P. Sudhindra, N. Roy and P. Paira, *Inorg. Chim. Acta*, 2020, **513**, 119925.

20 C. Pérez-Arnaiz, M. I. Acuña, N. Busto, I. Echevarría, M. Martínez-Alonso, G. Espino, B. García and F. Domínguez, *Eur. J. Med. Chem.*, 2018, **157**, 279–293.

21 M. Redrado, M. Miñana, M. P. Coogan, M. C. Gimeno and V. Fernández-Moreira, *ChemMedChem*, 2022, **17**, e202200244.

22 M. Redrado, E. Romanos, A. Benedi, G. Canudo-Barreras, I. Marzo, M. C. Gimeno and V. Fernández-Moreira, *Inorg. Chem. Front.*, 2024, **11**, 1828–1838.

23 W.-W. Qin, Z.-Y. Pan, D.-H. Cai, Y. Li and L. He, *Dalton Trans.*, 2020, **49**, 3562–3569.

24 Y. T. Lee, Y. J. Tan and C. E. Oon, *Acta Pharm. Sin. B*, 2023, **13**, 478–497.

25 E. Ortega-Forte, S. Hernández-García, G. Vigueras, P. Henarejos-Escudero, N. Cutillas, J. Ruiz and F. Gandía-Herrero, *Cell. Mol. Life Sci.*, 2022, **79**, 510.

26 J. Kasparkova, A. Hernández-García, H. Kostrhunova, M. Goicuría, V. Novohradsky, D. Bautista, L. Markova, M. D. Santana, V. Brabec and J. Ruiz, *J. Med. Chem.*, 2024, **67**, 691–708.

27 V. Novohradsky, G. Vigueras, J. Pracharova, N. Cutillas, C. Janiak, H. Kostrhunova, V. Brabec, J. Ruiz and J. Kasparkova, *Inorg. Chem. Front.*, 2019, **6**, 2500–2513.

28 L. He, Y. Li, C.-P. Tan, R.-R. Ye, M.-H. Chen, J.-J. Cao, L.-N. Ji and Z.-W. Mao, *Chem. Sci.*, 2015, **6**, 5409–5418.

29 S. Sil, A. Hussain, J. Das Sarma and P. Gupta, *ChemBioChem*, 2024, **25**, e202400597.

30 F.-X. Wang, M.-H. Chen, X.-Y. Hu, R.-R. Ye, C.-P. Tan, L.-N. Ji and Z.-W. Mao, *Sci. Rep.*, 2016, **6**, 38954.

31 P. Laha, U. De, F. Chandra, N. Dehury, S. Khullar, H. S. Kim and S. Patra, *Dalton Trans.*, 2018, **47**, 15873–15881.

32 K. Hasan, A. K. Bansal, I. D. W. Samuel, C. Roldán-Carmona, H. J. Bolink and E. Zysman-Colman, *Sci. Rep.*, 2015, **5**, 12325.

33 M. Ouyang, L. Zeng, K. Qiu, Y. Chen, L. Ji and H. Chao, *Eur. J. Inorg. Chem.*, 2017, **2017**, 1764–1771.

34 S. M. Mahalingam, J. D. Ordaz and P. S. Low, *ACS Omega*, 2018, **3**, 6066–6074.

35 R. Chebolu, D. N. Kommi, D. Kumar, N. Bollineni and A. K. Chakraborti, *J. Org. Chem.*, 2012, **77**, 10158–10167.

36 M. Nonoyama, *Bull. Chem. Soc. Jpn.*, 1974, **47**, 767–768.

37 A. I. Solomatina, K. M. Kuznetsov, V. V. Gurzhiy, V. V. Pavlovskiy, V. V. Porsev, R. A. Evarestov and S. P. Tunik, *Dalton Trans.*, 2020, **49**, 6751–6763.

38 E. Zafon, I. Echevarría, S. Barrabés, B. R. Manzano, F. A. Jalón, A. M. Rodríguez, A. Massaguer and G. Espino, *Dalton Trans.*, 2022, **51**, 111–128.

39 A. A. Gorman and M. A. J. Rodgers, *J. Photochem. Photobiol., B*, 1992, **14**, 159–176.

40 D. Ashen-Garry and M. Selke, *Photochem. Photobiol.*, 2014, **90**, 257–274.

41 M. S. Lowry, W. R. Hudson, R. A. Pascal and S. Bernhard, *J. Am. Chem. Soc.*, 2004, **126**, 14129–14135.

42 S. Amézqueta, X. Subirats, E. Fuguet, M. Rosés and C. Ràfols, in *Liquid-Phase Extraction*, Elsevier, 2020, pp. 183–208.

43 J. Sanz-Villafruela, C. Bermejo-Casadesus, E. Zafon, M. Martínez-Alonso, G. Durá, A. Heras, I. Soriano-Díaz, A. Giussani, E. Ortí, F. Tebar, G. Espino and A. Massaguer, *Eur. J. Med. Chem.*, 2024, **276**, 116618.

44 T. S.-M. Tang, K.-K. Leung, M.-W. Louie, H.-W. Liu, S. H. Cheng and K. K.-W. Lo, *Dalton Trans.*, 2015, **44**, 4945–4956.

45 A. Carreño, A. E. Aros, C. Otero, R. Polanco, M. Gacitúa, R. Arratia-Pérez and J. A. Fuentes, *New J. Chem.*, 2017, **41**, 2140–2147.

46 V. Fernández-Moreira, F. L. Thorp-Greenwood, A. J. Amoroso, J. Cable, J. B. Court, V. Gray, A. J. Hayes,

R. L. Jenkins, B. M. Kariuki, D. Lloyd, C. O. Millet, C. Ff. Williams and M. P. Coogan, *Org. Biomol. Chem.*, 2010, **8**, 3888.

47 A. Linero-Artiaga, L.-M. Servos, V. Rodríguez, J. Ruiz and J. Karges, *J. Med. Chem.*, 2025, **68**, 7792–7806.

48 K. Yusri, S. Jose, K. S. Vermeulen, T. C. M. Tan and V. Sorrentino, *NPJ Metab. Health Dis.*, 2025, **3**, 26.

49 A. K. Yadav, A. Upadhyay, A. Bera, R. Kushwaha, A. A. Mandal, S. Acharjee, A. Kunwar and S. Banerjee, *Inorg. Chem. Front.*, 2024, **11**, 5435–5448.

50 I. Ott, in *Comprehensive Inorganic Chemistry II*, Elsevier, 2013, pp. 933–949.

51 CCDC 2492431: Experimental Crystal Structure Determination, 2025, DOI: 10.5517/ccdc.csd.cc2pnl0z.